



Enhanced performance of FeOOH/ZnIn₂S₄/Au nanosheet arrays for visible light water splitting

Zhongyong Jiang^{1,2}, Kun Li^{1,2}, Xiaoyan Cai^{1,2}, Eugene Chubenko³, Vitaly Bondarenko³, Liang Mao^{1,2}, Yulong Zhao^{1,2,*}, and Xiuquan Gu^{1,2,*} 

¹ School of Materials Science and Physics, China University of Mining and Technology, Xuzhou 221116, People's Republic of China

² Jiangsu Province Engineering Laboratory of Highly Efficient Energy Storage Technology and Equipment, Xuzhou 221116, People's Republic of China

³ Belarusian State University of Informatics and Radioelectronics, 220013 P.Brovka str. 6, Minsk, Belarus

Received: 10 September 2021

Accepted: 22 December 2021

Published online:
3 February 2022

© The Author(s), under exclusive licence to Springer Science+Business Media, LLC, part of Springer Nature 2022

ABSTRACT

Carrier separation, charge transport, and visible light absorption are the main factors affecting the solar water splitting performance of a semiconductor photoanode. In this work, ZnIn₂S₄ (ZIS) nanosheet arrays (NSAs) were prepared by a hydrothermal route on a transparent fluorine-doped tin oxide (FTO) substrate, which was followed by a modification with an amorphous FeOOH thin layer. The surface morphology of ZIS NSAs was shown not to change regardless of whether Au was used as the seeding layer. Besides, the effect of the FeSO₄ solution concentration on the morphology, optical absorption, and photoelectrochemical (PEC) performance was investigated. The PEC measurements showed that at the 1.23 V bias relative to RHE (V_{RHE}), the FeOOH/ZIS/Au optical photoanodes exhibited a 4.5 and 1.9 times higher photocurrent density than the ZIS/FTO and ZIS/Au/FTO electrodes, respectively. For the 0.05Fe/ZIS/Au/FTO samples, the 0.91 mA cm⁻² initial photocurrent density was achieved at V_{RHE} of 1.23 V. The FeOOH/Au/ZIS photoanodes also displayed a maximum H₂ yield amount of 26.2 μmol cm⁻² h⁻¹. It was also observed that the enhanced PEC performance may be resulted from the synergistic effect of the FeOOH top decoration and Au under layer. Specifically, FeOOH facilitated the hole injection into the electrolyte, while Au NPs provided a number of sinks for the electron transport to the FTO substrates.

Address correspondence to E-mail: sdyulong@cumt.edu.cn; xqgu@cumt.edu.cn

1 Introduction

Energy crisis and acute environmental pollution issues have created considerable attention in the world with the continuous depletion of fossil fuels. The solar-driven photoelectrochemical (PEC) water splitting for the H₂ production by semiconductor photocatalysis has been considered as a promising and renewable strategy to solve the growing challenge of global energy in the near future [1, 2]. To this end, much research has been done to increase the efficiency of solar-to-hydrogen (STH) conversion, although the actual STH efficiency is well below practical requirements [3]. Still the main problem is the recombination of photogenerated carriers occurred at the semiconductor/electrolyte interface, which dramatically restrains the carrier concentration for the STH conversion.

Up to now, a lot of semiconductor photocatalysts, including BiVO₄, ZnO, WO₃, Bi₂MoO₆, CuInS₂, and BiOBr, have been attempted for constructing a solar response photoelectrode [4–9]. However, these materials either have a wide bandgap, which is not conducive to the solar harvesting, or they display poor stability and are vulnerable to photocorrosion. As a ternary transition metal sulfide, ZIS has recently attracted much attention in the field of photoelectric conversion since Li firstly reported the excellent photocatalytic activity of ZIS in the H₂ production [10]. ZIS not only has a suitable bandgap (2.5 eV) with a visible light response, but also displays a good chemical stability, especially in the acidic solution. We previously reported that ZIS was even used as a seeding layer (nucleation center) to produce ordered In₂S₃ NSAs [11].

Otherwise, surface morphology is also an important factor affecting the PEC performance of the photoelectrode. Generally speaking, the ideal photoelectrode should be one-dimensional (1D) or two-dimensional (2D) nanostructure arrays, which not only have a large specific surface area, but also possess a fast charge transport rate. Kar et al. have reported the growth and formation mechanism of vertically aligned arrays of copper sulfide nanostructures formed by electrochemical anodization. The CH₄ production rate reached as high as 38 μmol m⁻² h⁻¹ when these nanostructure arrays were used as stand-alone photocatalysts for the CO₂ photoreduction at room temperature [12]. The

nanostructured array not only provides an additional surface area to enable increased active reaction points, but also ensures a rapid charge separation while inhibiting the light harvesting loss. Finally, the semiconductor PEC performance can be enhanced by creating a heterojunction or *pn* junction. Xiao et al. have reported that a novel 2D/2D N-La₂Ti₂O₇/ZIS heterojunction showed a 5.2-fold high rate than ZIS for photocatalytic H₂-evolution, due to the unique 2D/2D heterojunction that promotes highly efficient charge transfer [13]. In addition, the cocatalyst modification has been an efficient method for enhancing the PEC activity of a semiconductor electrode [14]. Cocatalysts could not only lower the activation energy or overpotential for H₂- or O₂-evolution reactions on the surface of semiconductors, but also improve the stability of photoelectrodes by suppressing photocorrosion. It is generally accepted that Au refers to H₂-evolution cocatalysts, while the layered double hydroxide (such as NiOOH, FeOOH) is recognized as an O₂-evolution cocatalyst. Therefore, modifying Au at the surface of ZIS may not significantly enhance its photocurrent, while Au placed under ZIS may be conducive to enhance the electron collection and carrier separation. Manuel et al. have demonstrated the efficient harvesting of hot holes from Au nanoparticles (Au NPs) into amorphous TiO₂ performed near-exclusively by Au NPs. Photoanodes consisted of a single Au NPs layer of ~ 50 nm diameter coated with α-TiO₂ shell (Au@α-TiO₂) exhibited a photocurrent of 2.5 mA cm⁻² in 1 M KOH at an external bias of 0.6 V [15].

As far as we know, in many works hierarchical ZnIn₂S₄ NSAs were grown directly on FTO substrates or assisted by ZnO and TiO₂ seeding layers [16]. Au or other noble-metal NPs have often been used as the cocatalysts for enhancing the PEC activity of ZIS [11, 17], but there are no reports that Au NPs have been prepared on the FTO substrates to grow ZIS NSAs. According to a very recent report, single crystalline α-Fe₂O₃ nanoflakes (NFs) were formed in a highly dense array by Au seeding of a Fe substrate followed by a decoration with a thin FeOOH cocatalyst layer [18]. Such a α-Fe₂O₃/FeOOH NFs on Au/Fe photoanode yielded a photocurrent density of 3.1 mA·cm⁻² at 1.5 V_{RHE} under AM 1.5G (100 mW cm⁻²) simulated sunlight illumination.

In this work, the ZIS NSAs were modified with dual cocatalysts of FeOOH and Au NPs for the PEC water splitting. The introduction of Au NPs

promoted the enhanced absorption of visible light and electron collection, while the FeOOH modification facilitated the hole collection and accelerated the water oxidation reaction. After optimizing the parameters, the 0.05FeOOH/ZIS/Au photoanode displayed the initial photocurrent density of 0.31 mA cm^{-2} at $1.23 \text{ V}_{\text{RHE}}$, which was significantly higher than that of pure ZIS or ZIS/Au photoelectrodes. This work might be hopeful to provide new insights into designing a heterojunction photoanode for realizing a high-efficient solar conversion.

2 Experimental details

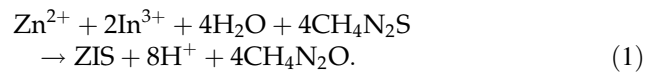
2.1 Electrodeposition of Au NPs onto FTO

First, the FTO-coated glass slices were cut into the same size ($2.5 \times 4 \text{ cm}$), then they were cleaned thoroughly in the distilled (DI) water, isopropyl alcohol, and ethanol (99%) for 30 min alternately and then dried for use. The Au NPs were prepared on the FTO glass substrates by a facile electrodeposition method using a 0.5 mM aqueous HAuCl_4 aqueous solution as the electrolyte. The electrodeposition process was carried out in a three-electrode cell with a FTO conductive substrate employed as the working electrode (WE), a saturated calomel electrode (SCE) as the reference electrode (RE), and a platinum (Pt) foil as the counter electrode (CE). During the electrodeposition, a bias of 0.1 V versus SCE ($0.1 \text{ V}_{\text{SCE}}$) was applied onto the WE for 120 s. Finally, the Au/FTO samples obtained were slowly rinsed with DI water and then dried in an oven.

2.2 Fabrication of ZIS/Au/FTO photoanodes

The ZIS/Au NSAs were prepared on the produced Au/FTO substrates by the simple hydrothermal method. A precursor solution was prepared by dissolving $0.2 \text{ mmol L}^{-1} \text{ ZnCl}_2$, $0.4 \text{ mmol L}^{-1} \text{ InCl}_3 \cdot 4\text{H}_2\text{O}$, and $1.6 \text{ mmol L}^{-1} \text{ CH}_3\text{CSNH}_2$ in 40 mL DI water followed by a magnetic stirring at room temperature (RT) for 20 min. Then, the resultant solution was transferred into a Teflon kettle, and two Au/FTO glass substrates were immersed into the solution with their conductive sides facing down. The Teflon kettle was sealed in an autoclave and kept at $180 \text{ }^\circ\text{C}$ for 3 h in an oven. After cooling down to RT, the ZIS NSA

samples were taken out, cleaned by DI water for 1 min, and dried at $60 \text{ }^\circ\text{C}$ in a vacuum oven. The reaction formula is represented as follows:



2.3 Modification of ZIS/Au/FTO photoanodes with FeOOH

For modifying with amorphous FeOOH, the ZIS/Au NSA photoanodes were immersed into the FeSO_4 solution of different concentrations (0.02, 0.05, 0.1, and 0.2 M) at RT for 24 h. The films obtained were marked as 0.02Fe/ZIS/Au, 0.05Fe/ZIS/Au, 0.1Fe/ZIS/Au, and 0.2Fe/ZIS/Au, respectively. In general, the technological steps for fabricating the FeOOH/ ZnIn_2S_4 /Au photoanode are shown in Figs. 1 and S1.

2.4 Materials characterization

Both the crystal and phase structures of the samples were examined by an X-ray diffractometer (XRD, ADVANCE, Bruker, Germany). The surface morphology and microstructure were determined by the field-emission scanning electron microscopy (FESEM, S-4800, Hitachi, made in Japan). The chemical composition and stoichiometry were evaluated by an energy-dispersive spectrometer (EDS). The fine microstructure of the samples was measured with a high-resolution transmission electron microscope (HRTEM) (Tecnai G2 F20). The optical absorption spectra were detected with a UV–vis spectrophotometer (Varian Cary 300) in the 300–800 nm range. Both the chemical composition and valence states were evaluated by the X-ray photoelectron spectroscopy (XPS, EscaLab 250Xi), while the PL spectra were recorded with a FS5 fluorescence spectrometer.

2.5 PEC measurements

The PEC tests were carried out with an electrochemical workstation (CHI660D) connected to a three-electrode cell under a simulated solar irradiation provided with a 500 W Xe lamp (Beijing Trustech Technology Co. Ltd.) equipped with an AM 1.5G filter, where the irradiation intensity was set as 100 mW/cm^2 . The as-prepared film samples (actual area of $2.5 \times 4 \text{ cm}$) were used as the WE, SCE was used as the RE, and the Pt foil was used as the CE, while three

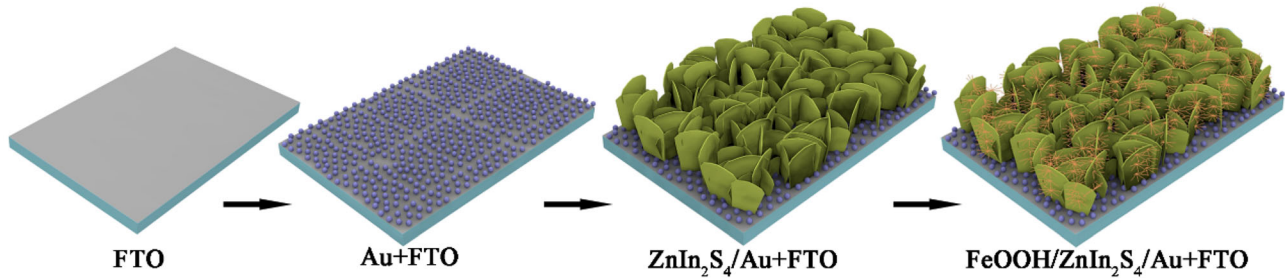


Fig. 1 Schematic illustration of the fabrication procedure of the FeOOH/ZnIn₂S₄/Au NSA photoanode

electrodes were immersed in the 0.1 M Na₂SO₄ aqueous solution (pH = 7.0). The transient photocurrent responses (*J*–*t* plots) were collected at a scan rate of 20 mV s^{−1}. The quantum efficiency (QE) was measured at 1.23 V_{RHE} by using a monochromatic LED as the irradiation source. Mott–Schottky (M–S) plots were measured in the dark at a constant frequency of 1 kHz, and time-dependent transient photocurrent (*J*–*t*) plots were collected under a chopped solar irradiation. In order to obtain the Nyquist plots, the electrochemical impedance spectra (EIS) were taken at 0.0 V_{SCE} with the frequency ranging from 0.1 Hz to 50 kHz under the solar irradiation with a 20 mV amplitude. The H₂-evolution rate was investigated in the 0.2 M Na₂SO₃ electrolyte at 1.23 V_{RHE} under AM 1.5 illumination (100 mW/cm²) by using an online gas chromatograph (Nexis GC-2030). The steady-state PL spectra were collected with a FS5 fluorescence spectrometer, while the time-resolved photoluminescence (TRPL) spectra were tested with FLS980. All the above measurements were carried out at room temperature (RT).

3 Results and discussion

Figure 2 compares the XRD patterns of ZnIn₂S₄/Au NSAs modified with different amounts of FeOOH. All the diffraction peaks are seen to be referred to the hexagonal phase of ZIS (JCPDS No. 65-2023), since the peaks at 27.69°, 30.45°, and 47.19° correspond to (102), (104), and (110) planes, respectively. Except the diffraction peaks from ZIS, the other peaks marked with the symbol were assigned to the FTO substrate. Notably, no peaks related to Au NPs and FeOOH were detected for the FeOOH/ZIS/Au NSA samples with various Fe contents, which may be due to the low amount of loaded Au or the amorphous nature of FeOOH. Of course, the absence of Au-related peaks

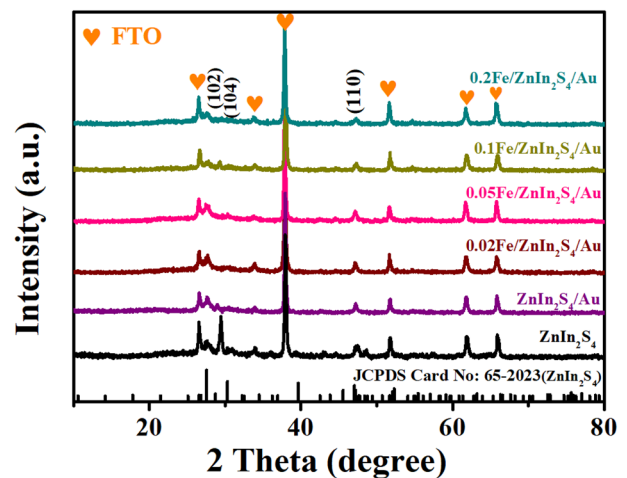


Fig. 2 XRD patterns of the as-synthesized ZIS and X-FeOOH/ZIS/Au electrodes (X represents the concentration of FeSO₄ aqueous solution)

may also be due to its location at the bottoms of ZIS NSAs. In addition, there is a gradual decrease in the intensity of the ZIS-related peaks with the increase in the FeSO₄ solution concentration, which might be associated with an increase in the thickness of the FeOOH layer that prevents the penetration of X-rays into the ZIS membranes.

Figure 3 displays the microscopic morphology of the samples after different growth stages or modified with different amounts of FeOOH. Figure 3a displays the high-resolution SEM image of Au/FTO and FTO (inset in Fig. 3a). It is clear that the Au NPs (red circle) with an average particle size of 10–50 nm can be seen to be uniformly distributed between the larger SnO₂ grains. Figure 3b shows the SEM image of ZIS NSA grown on the Au-seeded FTO substrate. The ZIS NSs are observed to be evenly distributed on the substrate with a small sheet thickness. There are no obvious differences between the SEM image of ZIS NSAs of this study and our earlier data [11, 19], suggesting that the presence of Au does not affect the

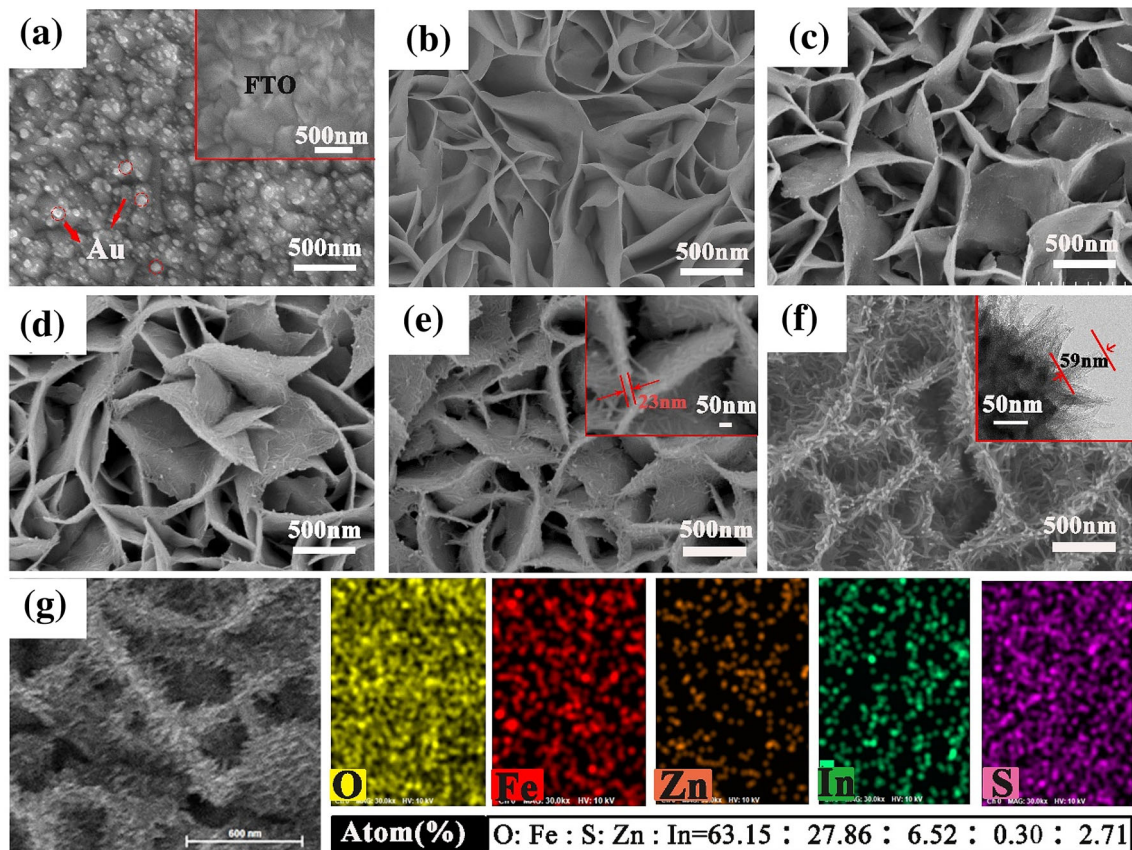


Fig. 3 FESEM images of **a** Au/FTO (inset: bare FTO), **b** ZIS/Au/FTO, **c** 0.02FeOOH/ZIS/Au, **d** 0.05FeOOH/ZIS/Au, **e** 0.1FeOOH/ZIS/Au (inset: higher magnification), **f** 0.2FeOOH/ZIS/Au (inset:

TEM image), **g** 0.2FeOOH/ZIS/Au and its corresponding EDS element mapping for O, Fe, Zn, In, and S

morphology of ZIS NSAs. Figure 3c–f shows the top-view SEM images of X-FeOOH/ZIS/Au photoanodes. It is worth noting that the FeOOH deposited at the low concentration of the FeSO_4 solution is distributed on the surface of ZIS NSs in the form of dots (Fig. 3c, d). With the increase of the solution concentration, the load of FeOOH also increases significantly, resulting in the formation of FeOOH NFs on the surface of ZIS NSs (Fig. 3e, f). Both the TEM images (inset in Fig. 3f) and the corresponding EDS pattern (Fig. S2) demonstrate the in situ formation of FeOOH NFs on the ZIS surface with an average length of 60 nm. Moreover, the EDS elemental mapping results are shown in Fig. 3g to confirm a homogeneous coverage of Fe over the entire ZIS surface. The relatively higher atomic content of Fe compared to Zn, In, and S indicates that FeOOH has completely covered the surface of ZIS membrane.

Figure 4 shows the XPS spectra of the samples to examine the chemical valence status and the elemental composition. The survey spectrum (Fig. 4a)

primarily shows the presence of Zn, In, S, Fe, and O along with small quantities of C and O from the absorbed species. This result confirms the existence of FeOOH, which is consistent with the EDS results described above. Nevertheless, Au element is absent in the XPS spectrum because Au particles are located under the ZIS film, while the Fe and O elements exist only in the FeOOH-modified sample. Besides, the peak intensity of FeOOH/ZIS/Au sample is significantly weaker than that of ZIS/Au because of a complete coating of amorphous FeOOH layer on the ZIS NSA. Figure 4b shows the O1s core-level spectrum, which consists of two peaks at 530.99 and 529.29 eV that correspond to the Fe–OH and Fe–O bonds, respectively [20]. In Fig. 4c, the Fe 2p consists of two peaks: Fe 2p_{1/2} and Fe 2p_{3/2}. Both are in good agreement with the two Gaussian peaks, suggesting the coexistence of Fe²⁺ and Fe³⁺ ions in the FeOOH amorphous layer [4]. As can be clearly seen from Fig. 4d, the binding energies of Zn 2p_{3/2} and Zn 2p_{1/2} are 1023.04 and 1046.14 eV, which is a typical

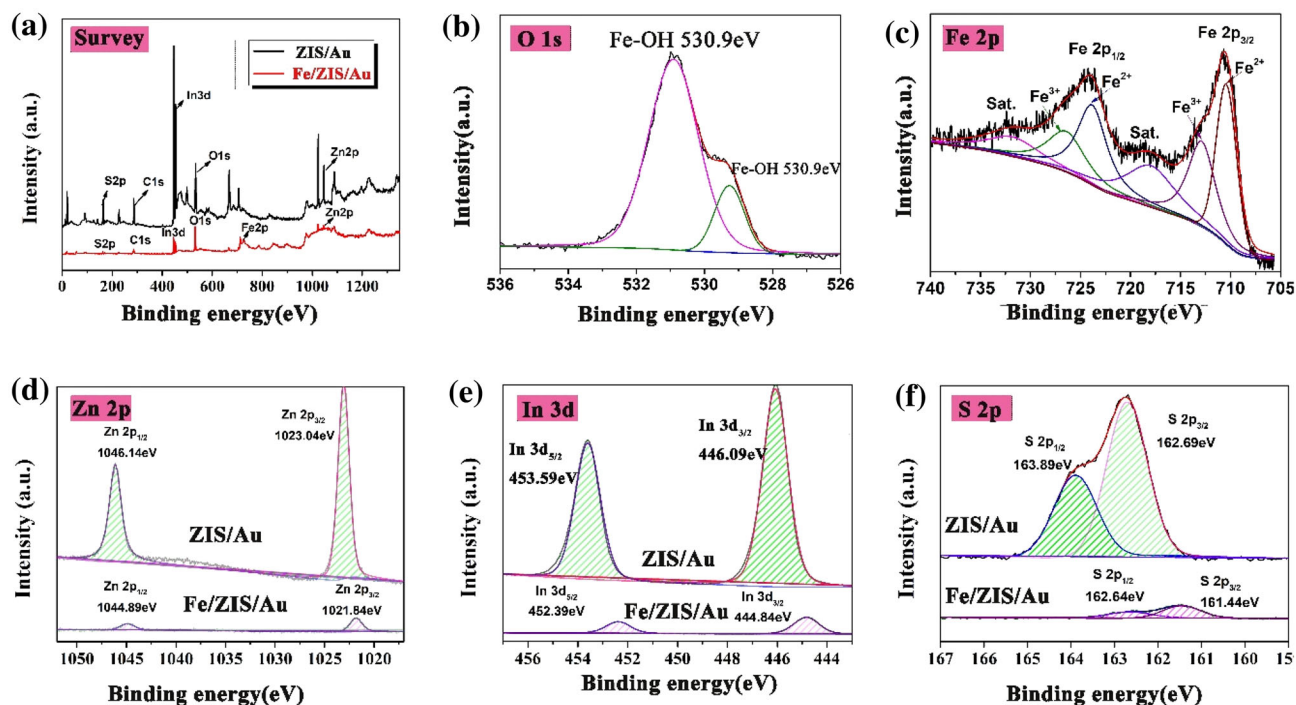


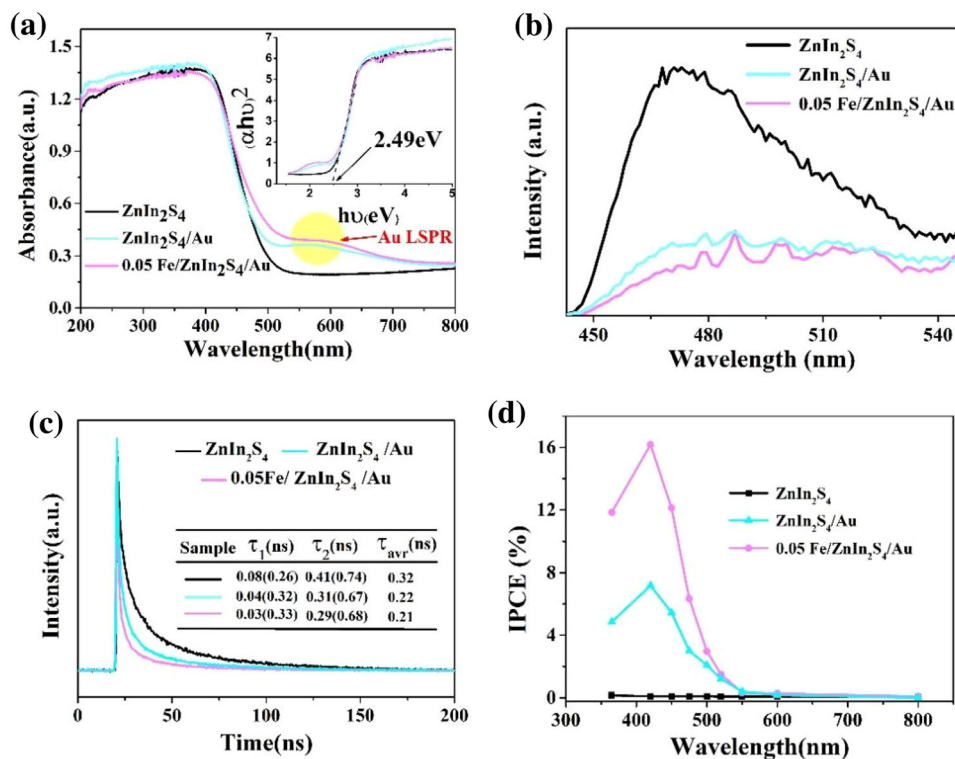
Fig. 4 XPS spectra of the electrodes ZIS/Au and 0.2Fe/ZIS/Au: **a** survey, core-level spectra of elements. **b** O 1s, **c** Fe 2p, **d** Zn 2p, **e** In 3d, and **f** S 2p

characteristic of Zn^{2+} ions located at the lattice of ZIS [21]. A pair of symmetrical peaks (Fig. 4e) located at 446.09 and 453.59 eV may be attributed to $\text{In } 3d_{3/2}$ and $\text{In } 3d_{5/2}$, which are indexed to the In–S bond [22]. The S 2p core level splits into two obvious peaks (Fig. 4f) with binding energies at 162.69 and 163.89 eV (corresponding to S $2p_{1/2}$ and S $2p_{3/2}$), confirming that the element S in ZIS exists in the form of the divalent chemical valence state [21]. The high-resolution spectrum of Au 4f (Fig. S4) showed two prominent peaks at 84.1 and 87.9 eV, corresponding to the Au $4f_{7/2}$ and Au $4f_{5/2}$, respectively. The chemical properties of Au in the modified ZIS sample are inferred to be metallic (Au^0) [23]. However, compared with ZIS/Au, the XPS characteristic peaks of Zn 2p, In 3d, and S 2p in FeOOH/ZIS/Au move towards the lower energy side, which might be attributed to the electron transfer from FeOOH to these elements in ZIS [5, 24, 25]. Such electron transfer is conducive to enhance the density of surrounding electron cloud, reducing the binding energy of these ions (Zn, In, and S).

Figure 5a compares the UV–vis absorption spectra of three samples ZIS, ZIS/Au, and 0.05FeOOH/ZIS/Au. Obviously, an abrupt absorption edge appears around 500 nm for these samples, corresponding to

their direct bandgap of ~ 2.49 eV. After loading Au NPs and FeOOH, the visible light absorption of ZIS is effectively promoted without any changes in their bandgap value (inset in Fig. 5a). It is worth noting that the broad absorption centered at 578 nm (yellow circle) is clearly observed for the two samples containing Au, which might be ascribed to the well-known local surface plasmon resonance (LSPR) effect [1, 2, 26]. The result further confirms the existence of Au NPs between ZIS and FTO, leading to an enhancement of visible light harvesting. Fig. S3a shows a comparison of the UV–vis absorption spectra of ZIS and X-FeOOH/ZIS/Au ($X = 0.02, 0.05, 0.1,$ and 0.2). The visible light absorption of the samples enhances with the increase in the FeOOH loading amounts, which may be ascribed to the narrower bandgap of the latter. The steady-state PL spectra of ZIS, ZIS/Au, and 0.05FeOOH/ZIS/Au are shown in Fig. 5b. Compared to the ZIS sample, the one after the modification displays a rapid PL quenching, suggesting that the recombination of photogenerated electron–hole pairs is effectively suppressed [27]. The loading of FeOOH facilitates the collection of photo-generated holes from the ZIS matrix, leading to a significant increase in the carrier separation efficiency (Fig. S3c).

Fig. 5 **a** UV–vis diffusion reflectance (the inset displays Tauc plots of these samples vs. photonic energy). **b** Steady-state PL spectra. **c** TRPL emission spectra. **d** IPCE curves



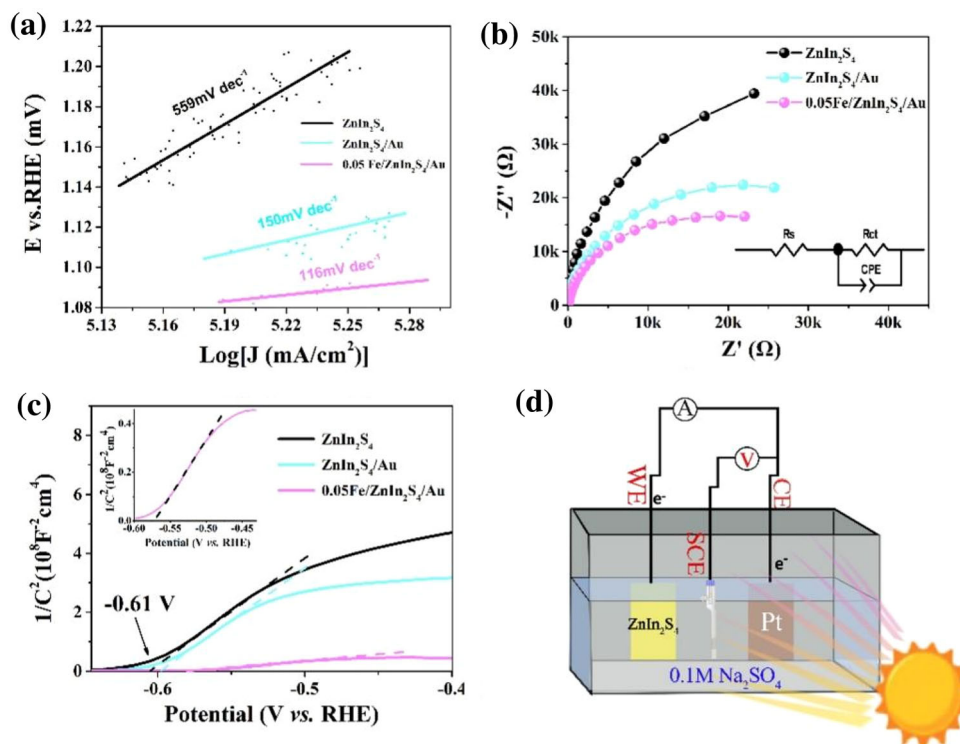
Next, we turned to the TRPL spectrum to investigate the charge carrier process as shown in Fig. 4g, fitting the decay curve using a double exponential decay model accompanied with a later slow decay (inset in Fig. 5d). The rapid decay (τ_1 , from 0.08 to 0.03 ns) might be ascribed to the fact that the electrons were trapped in the near-conduction-band-edge state as well as by the direct formation of free charge carriers. In contrast, the latter slow decay (τ_2 , from 0.41 to 0.29 ns) was attributed to the electron–hole recombination at the deeply trapped states or spatially localized states [28, 29]. Moreover, the intensity weighted lifetime (τ_{avr}) reduced from 0.32 ns for the pristine ZIS to 0.21 ns for the FeOOH/ZIS/Au, demonstrating that the appearance of the FeOOH/Au can promote favorable charge migration and inhibit the undesirable charge recombination at the ZIS surfaces. We then measured the incident photon to electron conversion efficiency (IPCE) for these photoanodes (Fig. 4a). When irradiated at 420 nm, the FeOOH/ZIS/Au photoanode exhibited higher QE value (16.2%) than the ZIS/Au (7.1%) and ZIS (0.3%) photoanodes.

Figure 6a shows the Tafel slopes of the electrodes. The FeOOH/ZIS/Au electrodes show a much lower Tafel slope value (116 mV dec⁻¹) than the

photoanodes ZIS/Au (150 mV dec⁻¹) and ZIS (559 mV dec⁻¹), indicating the decrease in the overpotential and a promotional effect of cocatalyst on the activity and kinetics of HER. To further elucidate the separation of photogenerated electrons and holes, the EIS data are displayed in Fig. 6b. It is observed that these Nyquist plots are in good agreement with the equivalent circuit model shown in the inset of Fig. 6b. Herein, R_{CT} and R_s correspond to the resistances from the solid/liquid interface and the solid electrode, respectively. It is well known that the smaller the radius, the faster the charge transfer at the electrode/electrolyte interface. The radius of the ZIS modified with FeOOH and Au NPs is the smallest, indicating that the synergistic effect of FeOOH and Au NPs increases the charge transfer and suppresses the charge recombination. The fitted results are listed in Table S1, which shows that the FeOOH/Au/ZIS has the lowest R_{CT} value (24.07 Ω) of all, suggesting that the interfacial charge transfer of the ZIS photoanode is enhanced after co-modifying with Au NPs and FeOOH cocatalyst.

As presented in Fig. 6c, the M–S plots are obtained at 1 kHz in the dark. The positive slope further indicates that these samples exhibit the n-type conduction behavior. The flat band potential (V_{FB}) value

Fig. 6 **a** Tafel slopes of ZnIn_2S_4 , $\text{ZnIn}_2\text{S}_4/\text{Au}$, and $0.05\text{FeOOH}/\text{ZnIn}_2\text{S}_4/\text{Au}$ towards HER. **b** EIS plots (the inset is an equivalent circuit model). **c** M–S plots at 1 kHz (the inset is a partial enlarged view of $0.05\text{FeOOH}/\text{ZIS}/\text{Au}$). **d** Schematic model of a three-electrode measurement system



moves towards the more positive side from -0.61 to $-0.58\text{ V}_{\text{RHE}}$ as a result of the joint modification of FeOOH and Au. It is well known that the more positive the V_{FB} value, the lower the Fermi-level (E_{F}) position is [30], which is approximately equivalent to its conduction band (CB) for an n-type semiconductor. Combined with the bandgap values obtained from Tauc plots (Fig. 5a), the valence band (VB) of the ZIS sample is situated at about $1.88\text{ V}_{\text{RHE}}$. The slope of this curve is inversely proportional to the photoanode carrier density (N_{d} , see the supporting literature for Formula 4), and the calculation results are represented in Table S1. Obviously, a noticeable 11-fold increase in the N_{D} value occurred after the co-modification of Au NPs and FeOOH, which contributes to improving the conductivity of ZIS and triggering the water oxidation reaction.

The LSV curves for ZIS, Au/ZIS, and FeOOH/ZIS/Au were compared, as shown in Fig. 7a. All the samples displayed good photoresponse and photosensitivity. Obviously, the highest PEC activity was obtained in the FeOOH/ZIS/Au and it showed a superior photocurrent density of 0.91 mA cm^{-2} at $1.23\text{ V}_{\text{RHE}}$, which was 4.5 times higher than that of the pristine ZIS photoanode. Figure 6b compares the transient photocurrent responses of the photoanodes

studied by the chronoamperometric current method at $1.23\text{ V}_{\text{RHE}}$ under illumination with chopping. It is noted that ZIS NSA directly deposited on the FTO substrate displays a poor photocurrent density of 0.22 mA cm^{-2} , which increases to 0.51 mA cm^{-2} after the Au NPs deposition on the FTO bottom. The photocurrent density can be further enhanced to 0.91 mA cm^{-2} after modifying with FeOOH. In other words, the FeOOH/ZIS/Au sample shows an almost two-fold increase in photocurrent compared to the ZIS/Au sample. In addition, for the ZIS/Au and FeOOH/ZIS/Au electrodes, a series of sharp transient spike was observed when the light barrier is removed, because the photogenerated holes accumulate at the electrode–electrolyte interface and then recombine with the photogenerated electrons [31]. In contrast, almost no spike appears on the ZIS electrode, but its photocurrent value is rather low. The reason why the FeOOH decorated electrode samples display poor stability remains unknown.

In addition, the influence of the FeOOH loading amounts on the actual PEC performance of ZIS/Au electrodes was investigated. As shown in Fig. S4a, the ZIS displays the negligible photocurrent density under irradiation. As the FeOOH loading increases, the photocurrent density gradually improves,

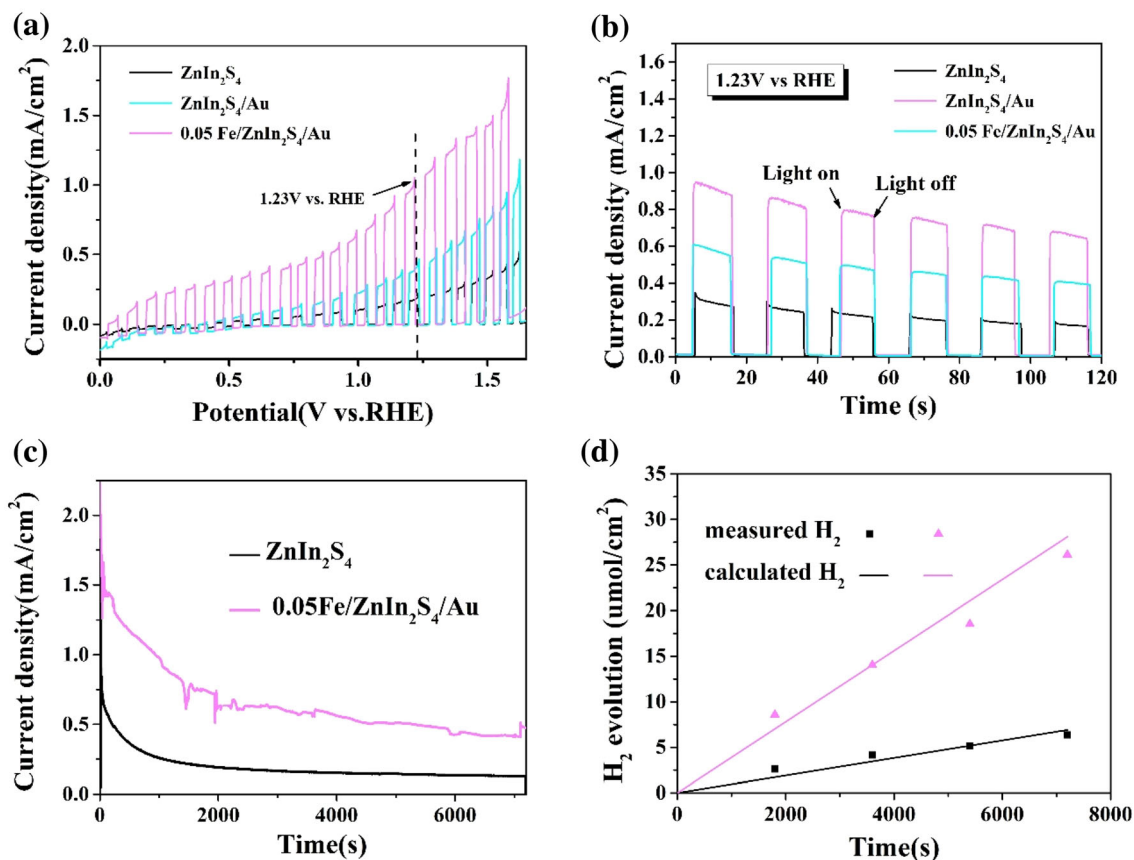


Fig. 7 LSV plots under a chopped irradiation (a). Amperometric *i*-*t* curves at 1.23 V_{RHE} under standard AM 1.5 G solar light illumination (b). *J*-*t* plots (c) and time course for PEC H₂-evolution (d) of ZnIn₂S₄, ZnIn₂S₄/Au, and 0.05FeOOH/ZnIn₂S₄/Au

reaching a maximum value of 0.91 mA cm⁻² on the 0.05FeOOH/ZIS/Au photoelectrode under 1.23 V_{RHE}. Nevertheless, the photocurrent decreases when the proportion of FeOOH continues to increase. It might be ascribed to the active sites blocking after the excessive ZIS loading, which further reduces the PEC performance [32]. The Nyquist plots (Fig. S4b) of 0.05FeOOH/ZIS/Au exhibits a smaller arc radius than samples of other concentrations, indicating a faster charge transfer. Additionally, the M-S plots of X-FeOOH/ZIS/Au are displayed in Fig. S4c. As analyzed above, the highest carrier density belongs to the 0.05FeOOH/ZIS/Au, and the V_{FB} position shifts towards the more positive side when the FeSO₄ concentration in the solution is increased to 0.05 M. As a result, the optimal concentration should be 0.05 M for the immersion of ZIS or ZIS/Au into the FeSO₄ solution.

The PEC activities of all the photoanodes were evaluated by measuring the photocurrent density over time (*J*-*t*) at 1.23 V_{RHE} under prolonged AM 1.5

G illumination. As presented in Fig. 7c, the pristine ZIS showed the relatively low photocurrent density and a slight downward trend. When the Au NPs or FeOOH were loaded, the ZIS showed the significantly increased photocurrent density. Meanwhile, the Faraday efficiency for the water splitting was detected by a gas chromatography (GC) quantitatively (Fig. 8d). Compared to the calculated theoretical data, the actually measured H₂ yield was relatively low, with a Faraday efficiency of approximately 92%. In addition, it was also revealed that the amount of H₂ increased linearly with prolonging light irradiation time. After irradiation for 2 h, the amount of generated H₂ on the FeOOH/ZIS/Au photoanode reached 26.29 μmol, which was 4 times higher than that on the ZIS photoanode.

Based on the above analysis, Fig. 8 suggests a possible mechanism to explain the enhancement of PEC activity caused by co-modification of Au NPs and FeOOH. First, the visible light absorption could be enhanced by coupling with plasmonic Au NPs via

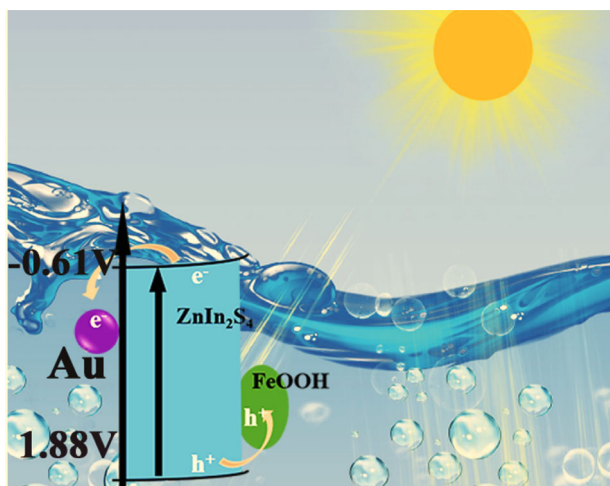


Fig. 8 Schematic illustration of a PEC water splitting cell

the local field enhancement effect [33]. Namely, the modification of Au NPs broadens the visible light absorption range of ZIS (Fig. 5a) [7]. Second, a multitude of electron–hole pairs are generated inside the ZIS NSAs [34–36]. Apparently, the surface modification with FeOOH contributes to the accumulation of holes for water oxidization, and the presence of Au NPs on the other side contributes to the electron collection by the FTO substrate.

4 Conclusion

In summary, a novel ZnIn_2S_4 NSA consisted of needle-like FeOOH NFs at the surface and Au NPs underlying the NSA was fabricated on the FTO-coated substrates by a facile immersion/electrodeposition method. The effects of the FeOOH loading amounts on the PEC performance of the FeOOH/ZIS/Au photocathodes were investigated. After the optimization, the 0.05FeOOH/Au/ZIS photoanode displayed a high initial photocurrent density (0.91 mA cm^{-2} at $1.23 V_{\text{RHE}}$), which was 4.5 times higher than that of the pristine ZIS photoanode. The enhanced PEC activity might be attributed to an improvement in both the visible light absorption and the carrier separation. Specifically, the amorphous FeOOH cocatalyst accumulates holes for water oxidization, and Au NPs contribute to the electron collection for the FTO substrate. This work might provide a new idea for designing high-efficient PEC water splitting anodes in the near future.

Acknowledgements

This work is financially supported by the Fundamental Research Funds for the Central Universities (2019ZDPY04).

Author contributions

ZJ: Preparation of materials, methodology, and software. KL: preparation of materials. XC: data curation and writing—original draft preparation. EC: writing—reviewing and editing. VB: XPS result analysis. LM: software, theoretical calculation, and validation. YZ: SEM and TEM measurements. XG: supervision, writing—reviewing and editing.

Data availability

The data that support the findings of this study are openly available to the reviewers.

Declarations

Conflict of interest The authors declare that they have no known competing financial interests or personal relationships that could have appeared to influence the work reported in this paper.

Supplementary Information: The online version contains supplementary material available at <http://doi.org/10.1007/s10854-022-07785-x>.

References

1. S. Linic, P. Christopher, D.B. Ingram, Plasmonic-metal nanostructures for efficient conversion of solar to chemical energy. *Nat. Mater.* **10**(12), 911–921 (2011)
2. D. Guo, H.-F. Wei, X.-Y. Yu, Q. Xia, Z. Chen, J.-R. Zhang, R.-B. Song, J.-J. Zhu, Plasmon-enhanced cathodic reduction for accelerating electricity generation in visible-light-assisted microbial fuel cells. *Nano Energy* **57**, 94–100 (2019)
3. T. Higashi, H. Nishiyama, Y. Suzuki, Y. Sasaki, T. Hisatomi, M. Katayama, T. Minegishi, K. Seki, T. Yamada, K. Domen, Transparent Ta_3N_5 photoanodes for efficient oxygen evolution toward the development of tandem cells. *Angew. Chem. Int. Ed.* **58**, 2300–2304 (2019)
4. W. Zhang, J. Ma, L. Xiong, H.-Y. Jiang, J. Tang, Well-crystallized α -FeOOH cocatalysts modified BiVO_4 photoanodes

- for efficient and stable photoelectrochemical water splitting. *ACS Appl. Energy Mater.* **3**(6), 5927–5936 (2020)
5. C. Liu, Y. Qiu, F. Wang, L. Li, Q. Liang, Z. Chen, Electrodeposition of ZnO nanoflake-based photoanode sensitized by carbon quantum dots for photoelectrochemical water oxidation. *Ceram. Int.* **43**(6), 5329–5333 (2017)
 6. J. Su, L. Guo, N. Bao, C.A. Grimes, Nanostructured WO₃/BiVO₄ heterojunction films for efficient photoelectrochemical water splitting. *Nano Lett.* **11**, 1928–1933 (2011)
 7. L. Guo, Q. Zhao, Y.C. Zhang, Y.Y. Zhang, X.X. Han, K.L. Zhang, D.J. Wang, F. Fu, Design and construction of all-solid Z-scheme CdS/Au/Bi₂MoO₆ heterostructure with enhanced photocatalytic performance. *Chin. J. Inorg. Chem.* **36**(1), 11–20 (2020)
 8. X.L. Tu, M. Li, Y.J. Su, G.L. Yin, J. Lu, D.N. He, Self-templated growth of CuInS₂ nanosheet arrays for photoelectrochemical water splitting. *J. Alloys Compd.* **809**, 1541794 (2020)
 9. K. Gao, X. Bai, Y. Zhang, Y.T. Ji, N-doped graphene quantum dots embedded in BiOBr nanosheets as hybrid thin film electrode for quantitative photoelectrochemical detection paracetamol. *Electrochim. Acta* **318**, 422–429 (2019)
 10. M.T. Li, J.Z. Su, L.J. Guo, Preparation and characterization of ZnIn₂S₄ thin films deposited by spray pyrolysis for hydrogen production. *Int. J. Hydrog. Energy* **33**, 2891–2896 (2008)
 11. K. Li, X.Y. Cai, Y.L. Zhao, X.Q. Gu, L. Mao, Fabrication of ZnIn₂S₄/Au nanosheet arrays for visible-light-response photoelectrochemical N₂ fixation, *Chinese. J. Inorg. Chem.* **36**, 2179–2188 (2021)
 12. P. Kar, S. Farsinezhad, X. Zhang, K. Shankar, Anodic Cu₂S and CuS nanorod and nanowall arrays: preparation, properties and application in CO₂ photoreduction. *Nanoscale* **6**(23), 14305–14318 (2014)
 13. M. Xiao, X. Yan, H. Li, N. Wells, G. Yang, Well-designed efficient charge separation in 2D/2D N doped La₂Ti₂O₇/ZnIn₂S₄ heterojunction through band structure/morphology regulation synergistic effect. *Nano Energy* **78**, 105401 (2020)
 14. J.R. Ran, J. Zhang, J.G. Yu, M. Jaroniec, S.Z. Qiao, Earth-abundant cocatalysts for semiconductor based photocatalytic water splitting. *Chem. Soc. Rev.* **43**, 7787–7812 (2014)
 15. E. Vahidzadeh, S. Zeng, K.M. Alam, P. Kumar, S. Riddell, N. Chaulagain, S. Gusarov, A.E. Kobryn, K. Shankar, Harvesting hot holes in plasmon-coupled ultrathin photoanodes for high-performance photoelectrochemical water splitting. *ACS Appl. Mater. Interfaces* **13**(36), 42741–42752 (2021)
 16. B. Fan, Z.H. Chen, Q. Liu, Z.G. Zhang, X.M. Fang, One-pot hydrothermal synthesis of Ni-doped ZnIn₂S₄ nanostructured film photoelectrodes with enhanced photoelectrochemical performance. *Appl. Surf. Sci.* **370**, 252–259 (2016)
 17. H.Q. An, Z.T. Lv, K. Zhang, C.Y. Deng, H. Wang, Z.W. Xu, M.R. Wang, Z. Yin, Plasmonic coupling enhancement of core-shell Au@Pt assemblies on ZnIn₂S₄ nanosheets towards photocatalytic H₂ production. *Appl. Surf. Sci.* **536**, 147934 (2021)
 18. L. Wang, N.T. Nguyen, Y.J. Zhang, Y.P. Bi, P. Schmuki, Enhanced solar water splitting by swift charge separation in Au/FeOOH sandwiched single crystalline Fe₂O₃ nanoflake photoelectrodes. *Chemsuschem* **10**, 2720–2727 (2017)
 19. L.M. Wang, M. Wei, X.Q. Gu, Y.L. Zhao, Y.H. Qiang, Preparation, photoelectrochemical properties and biosensor applications of oriented 2-D ZnIn₂S₄ nanosheet arrays for detecting glutathione (GSH). *J. Electron. Mater.* **47**, 6540–6550 (2018)
 20. Y. Jia, T. Luo, X.-Y. Yu, B. Sun, J.-H. Liu, X.-J. Huang, Synthesis of monodispersed α-FeOOH nanorods with a high content of surface hydroxyl groups and enhanced ion-exchange properties towards As(V). *RSC Adv.* **3**(36), 15805–15811 (2013)
 21. X. Tu, J. Lu, M. Li, Y. Su, G. Yin, D. He, Hierarchically ZnIn₂S₄ nanosheet-constructed microwire arrays: template-free synthesis and excellent photocatalytic performances. *Nanoscale* **10**(10), 4735–4744 (2018)
 22. Q. Tian, W. Wu, J. Liu, Z. Wu, W. Yao, J. Ding, C. Jiang, Dimensional heterostructures of 1D CdS/2D ZnIn₂S₄ composited with 2D graphene: designed synthesis and superior photocatalytic performance. *Dalton Trans.* **46**(9), 2770–2777 (2017)
 23. J. Li, C.-Y. Liu, Y. Liu, Au/graphene hydrogel: synthesis, characterization and its use for catalytic reduction of 4-nitrophenol. *J. Mater. Chem.* **22**(17), 8426 (2012)
 24. T. Zhou, S. Chen, J. Wang, Y. Zhang, J. Li, J. Bai, B. Zhou, Dramatically enhanced solar-driven water splitting of BiVO₄ photoanode via strengthening hole transfer and light harvesting by co-modification of CQDs and ultrathin β-FeOOH layers. *Chem. Eng. J.* **403**, 126350 (2021)
 25. L. Zhang, H. Li, B. Yang, N. Han, Y. Wang, Z. Zhang, Y. Zhou, D. Chen, Y. Gao, Promote the electrocatalysis activity of amorphous FeOOH to oxygen evolution reaction by coupling with ZnO nanorod array. *J. Solid State Electrochem.* **24**(4), 905–914 (2020)
 26. G. Zhang, X. Zhu, D. Chen, N. Li, Q. Xu, H. Li, J. He, H. Xu, J. Lu, Hierarchical Z-scheme g-C₃N₄/Au/ZnIn₂S₄ photocatalyst for highly enhanced visible-light photocatalytic nitric oxide removal and carbon dioxide conversion. *Environ. Sci.* **7**(2), 676–687 (2020)
 27. T. Mokari, E. Rothenberg, I. Popov, R. Costi, U. Banin, Selective growth of metal tips onto semiconductor quantum rods and tetrapods. *Science* **304**(5678), 1787–1790 (2004)

28. J.K. Kim, Y. Cho, M.J. Jeong, B. Levy-Wendt, D. Shin, Y. Yi, D.H. Wang, X. Zheng, J.H. Park, Rapid formation of a disordered layer on monoclinic BiVO₄: Co-catalyst-free photoelectrochemical solar water splitting. *Chemsuschem* **11**(5), 933–940 (2018)
29. H.L. Tan, X. Wen, R. Amal, Y.H. Ng, BiVO₄ 010 and {110} relative exposure extent: governing factor of surface charge population and photocatalytic activity. *J. Phys. Chem. Lett.* **7**(7), 1400–1405 (2016)
30. L.M. Wang, X.Q. Gu, Y.L. Zhao, M. Wei, Y.H. Qiang, Y. Zhao, Enhanced photoelectrochemical performance by doping Mo into BiVO₄ lattice. *J. Mater. Sci.* **29**(22), 19278–19286 (2018)
31. H. Qian, Z. Liu, Z. Guo, M. Ruan, J. Ma, Hexagonal phase/cubic phase homogeneous ZnIn₂S₄ n-n junction photoanode for efficient photoelectrochemical water splitting. *J. Alloys Compds.* **830**, 154639 (2020)
32. X. Zhao, Y. Fan, W. Zhang, X. Zhang, D. Han, L. Niu, A. Ivaska, Nanoengineering construction of Cu₂O nanowire arrays encapsulated with g-C₃N₄ as 3D spatial reticulation all-solid-state direct Z-scheme photocatalysts for photocatalytic reduction of carbon dioxide. *ACS Catal.* **10**(11), 6367–6376 (2020)
33. Y. Qu, R. Cheng, Q. Su, X. Duan, Plasmonic enhancements of photocatalytic activity of Pt/n-Si/Ag photodiodes using Au/Ag core/shell nanorods. *J. Am. Chem. Soc.* **133**(42), 16730–16733 (2011)
34. S.T.M. Michael, R. Hoffmann, W. Choi, D.W. Bahnemann, Environmental applications of semiconductor photocatalysis. *Chem. Rev.* **95**(1), 69–96 (1994)
35. X.Z. Li, F.B. Li, Study of Au/Au³⁺-TiO₂ photocatalysts toward visible photooxidation for water and wastewater treatment. *Environ. Sci. Technol.* **35**(2001), 2381–2387 (2001)
36. A.P. Manuel, A. Kirkey, N. Mahdi, K. Shankar, Plexcitonics—fundamental principles and optoelectronic applications. *J. Mater. Chem. C* **7**(7), 1821–1853 (2019)

Publisher's Note Springer Nature remains neutral with regard to jurisdictional claims in published maps and institutional affiliations.

Terms and Conditions

Springer Nature journal content, brought to you courtesy of Springer Nature Customer Service Center GmbH (“Springer Nature”).

Springer Nature supports a reasonable amount of sharing of research papers by authors, subscribers and authorised users (“Users”), for small-scale personal, non-commercial use provided that all copyright, trade and service marks and other proprietary notices are maintained. By accessing, sharing, receiving or otherwise using the Springer Nature journal content you agree to these terms of use (“Terms”). For these purposes, Springer Nature considers academic use (by researchers and students) to be non-commercial.

These Terms are supplementary and will apply in addition to any applicable website terms and conditions, a relevant site licence or a personal subscription. These Terms will prevail over any conflict or ambiguity with regards to the relevant terms, a site licence or a personal subscription (to the extent of the conflict or ambiguity only). For Creative Commons-licensed articles, the terms of the Creative Commons license used will apply.

We collect and use personal data to provide access to the Springer Nature journal content. We may also use these personal data internally within ResearchGate and Springer Nature and as agreed share it, in an anonymised way, for purposes of tracking, analysis and reporting. We will not otherwise disclose your personal data outside the ResearchGate or the Springer Nature group of companies unless we have your permission as detailed in the Privacy Policy.

While Users may use the Springer Nature journal content for small scale, personal non-commercial use, it is important to note that Users may not:

1. use such content for the purpose of providing other users with access on a regular or large scale basis or as a means to circumvent access control;
2. use such content where to do so would be considered a criminal or statutory offence in any jurisdiction, or gives rise to civil liability, or is otherwise unlawful;
3. falsely or misleadingly imply or suggest endorsement, approval, sponsorship, or association unless explicitly agreed to by Springer Nature in writing;
4. use bots or other automated methods to access the content or redirect messages
5. override any security feature or exclusionary protocol; or
6. share the content in order to create substitute for Springer Nature products or services or a systematic database of Springer Nature journal content.

In line with the restriction against commercial use, Springer Nature does not permit the creation of a product or service that creates revenue, royalties, rent or income from our content or its inclusion as part of a paid for service or for other commercial gain. Springer Nature journal content cannot be used for inter-library loans and librarians may not upload Springer Nature journal content on a large scale into their, or any other, institutional repository.

These terms of use are reviewed regularly and may be amended at any time. Springer Nature is not obligated to publish any information or content on this website and may remove it or features or functionality at our sole discretion, at any time with or without notice. Springer Nature may revoke this licence to you at any time and remove access to any copies of the Springer Nature journal content which have been saved.

To the fullest extent permitted by law, Springer Nature makes no warranties, representations or guarantees to Users, either express or implied with respect to the Springer nature journal content and all parties disclaim and waive any implied warranties or warranties imposed by law, including merchantability or fitness for any particular purpose.

Please note that these rights do not automatically extend to content, data or other material published by Springer Nature that may be licensed from third parties.

If you would like to use or distribute our Springer Nature journal content to a wider audience or on a regular basis or in any other manner not expressly permitted by these Terms, please contact Springer Nature at

onlineservice@springernature.com